A&A 681, A40 (2024)
https://doi.org/10.1051/0004-6361/202347202

Astronomy & Astrophysics

Probing the face-on disc-corona system of the bare AGN Mrk 110 from UV to hard X-rays: A moderate changing-state AGN?

D. Porquet[1], S. Hagen[2], N. Grosso[1], A. Lobban[3], J. N. Reeves[4,5], V. Braito[5,4,6], and C. Done[2]

[1] Aix-Marseille Univ, CNRS, CNES, LAM, Marseille, France
e-mail: delphine.porquet@lam.fr
[2] Centre for Extragalactic Astronomy, Department of Physics, Durham University, South Road, Durham DH1 3LE, UK
[3] European Space Agency (ESA), European Space Astronomy Centre (ESAC), 28691 Villanueva de la Cañada, Madrid, Spain
[4] Department of Physics, Institute for Astrophysics and Computational Sciences, The Catholic University of America, Washington, DC 20064, USA
[5] INAF, Osservatorio Astronomico di Brera, Via Bianchi 46, 23807 Merate (LC), Italy
[6] Dipartimento di Fisica, Università di Trento, Via Sommarive 14, Trento 38123, Italy

Received 15 June 2023 / Accepted 20 October 2023

ABSTRACT

Context. The X-ray broadband spectra of the bare active galactic nucleus (AGN) Mrk 110, obtained by simultaneous *XMM-Newton* and *NuSTAR* observations performed in November 2019 and April 2020, are characterised by the presence of a prominent and absorption-free smooth soft X-ray excess, moderately broad O VII and Fe Kα emission lines, and a lack of a strong Compton hump. The disc-corona system is almost viewed face-on as inferred from the O VII accretion disc lines. While relativistic reflection as the sole emission is ruled out, a simplified combination of soft and hard Comptonisation (using COMPTT) from a warm and a hot corona, plus mild relativistic disc reflection (occuring at a few 10 s R_g) reproduces the data very well.
Aims. We aim to confirm the physical origin of the soft X-ray excess of Mrk 110 and to determine its disc-corona system properties from its energetics using two new sophisticated models: REXCOR and RELAGN, respectively.
Methods. We applied these models to the 0.3–79 keV X-ray broadband spectra and to the spectral energy distribution (SED) from UV to hard X-rays, respectively.
Results. At both epochs, the inferred high values of the warm-corona heating from the X-ray broadband spectral analysis using REXCOR confirm that the soft X-ray excess of Mrk 110 mainly originates from a warm corona rather than relativistic reflection. The intrinsic best-fit SED determined at both epochs using RELAGN show a high X-ray contribution relative to the UV and are very well reproduced by a warm and hot corona plus mild relativistic reflection. The outer radii of the hot and warm corona are located at a few 10 s and ~100 R_g, respectively. Moreover, combining the inferred low Eddington ratio (approximatively a few percent) from this work, and previous multi-wavelength spectral and timing studies suggest that Mrk 110 could be classified as a moderate changing-state AGN.
Conclusions. Our analysis confirms the existence of a warm corona as a significant contribution to the soft X-ray excess and UV emission in Mrk 110, adding to growing evidence that AGN accretion deviates from standard disc theory. This strengthens the importance of long-term multi-wavelength monitoring on both single targets and large AGN surveys to reveal the real nature of the disc-corona system in AGNs.

Key words. X-rays: individuals: Mrk 110 – galaxies: active – quasars: general – radiation mechanisms: general – accretion, accretion disks

1. Introduction

In the standard picture, the emission of an AGN stems from an accretion disc around a supermassive black hole (SMBH) with masses spanning from a few million to billions of solar masses. X-ray spectra allow us to probe the geometry and the main physical process(es) at work in the inner part of the disc-corona system: for example, relativistic reflection resulting from the illumination of the standard accretion disc by a hot corona and/or Comptonisation of seed photons from the accretion disc by a warm-hot corona (e.g., Magdziarz et al. 1998; Porquet et al. 2004, 2018; Crummy et al. 2006; Bianchi et al. 2009; Fabian et al. 2012; Done et al. 2012; Petrucci et al. 2018; Gliozzi & Williams 2020; Waddell & Gallo 2020).

A large fraction of AGNs exhibit warm absorbers along the line of sight (e.g., Porquet et al. 2004; Piconcelli et al. 2005; Tombesi et al. 2013; Laha et al. 2014) which can severely bias the X-ray data analysis. Therefore, bare AGNs that show no (or very weak) X-ray warm absorbers are the best targets for directly investigating the process(es) at work in disc-corona systems around SMBHs. Very high signal-to-noise ratio data from simultaneous X-ray broadband observations of bright bare AGNs with *XMM-Newton* and *NuSTAR* offer us the possibility to determine the dominant physical process(es) at work, as performed, for instance, for the broad-line Seyfert 1 (BLS1) Ark 120 (Matt et al. 2014; Porquet et al. 2018, 2019) and the narrow-line Seyfert 1 (NLS1) TON S180 (Matzeu et al. 2020). These deep X-ray observations allow us to rule out, for these two AGNs, relativistic reflection from a constant-density, flat, standard accretion disc as the sole emission process. Indeed, this emission process cannot, regardless the hot-corona geometry, simultaneously reproduce the soft X-ray excess, the broad

Fe Kα complex, and the hard X-ray shape. Instead, the X-ray broadband spectra of these two AGNs are very well reproduced by a combination of soft and hard Comptonisation from a warm and hot corona, respectively, plus mild relativistic disc reflection.

Mrk 110 (also known as PG 0921+525) is a bright, type 1 Seyfert galaxy in the local Universe (z = 0.035291), with a bolometric luminosity of about 5×10^{44} erg s^{-1} (Woo & Urry 2002). This source is radio-quiet but not radio-silent (Xu et al. 1999; Miller et al. 1993; Kukula et al. 1998; Järvelä et al. 2022; Panessa et al. 2022; Chen et al. 2022). From optical observations, its type E host galaxy displays a disturbed morphology with a significant tidal tail which could suggest a past merger or tidal interaction with only one apparent nucleus (Adams 1977; Wehinger & Wyckoff 1977; Hutchings & Craven 1988; MacKenty 1990; Bischoff & Kollatschny 1999). Moreover, both its optical continuum and broad lines are strongly variable on days-to-year time-scales (Peterson et al. 1984, 1998; Bischoff & Kollatschny 1999; Kollatschny et al. 2001; Homan et al. 2023). In X-rays, Mrk 110 exhibits flux variations by a factor of up to ∼4–5 on yearly time-scales, as observed by long-term observations with the *Rossi* X-ray Timing Explorer (RXTE; e.g., Markowitz & Edelson 2004; Weng et al. 2020).

This source is frequently classified as a NLS1 when only considering the measurements of a relatively narrow optical Hβ emission line with a full width at half maximum (FWHM) of ∼1700–2500 km s^{-1}, emitted by its broad-line region (BLR; Osterbrock 1977; Peterson et al. 1984; Crenshaw 1986; Bischoff & Kollatschny 1999; Vestergaard 2002; Grupe et al. 2004). However, Mrk 110 displays much broader and more redshifted optical BLR components from Balmer lines (Hα, Hβ, and Hγ), He I$\lambda\lambda$5876,6678 and He IIλ4686 lines ($FWHM$ ∼ 5000–6000 km s^{-1}; Bischoff & Kollatschny 1999; Véron-Cetty et al. 2007), as well as an unusually large [O III]λ5007/Hβ ratio and very weak Fe II emission (Boroson & Green 1992; Grupe et al. 2004; Véron-Cetty et al. 2007). Therefore, these properties are more consistent with a BLS1. This is strengthened by the X-ray timing and spectral characteristics of Mrk 110 which are similar to those found for moderate accretion-rate BLS1s (Porquet et al. 2004, 2021; Boller et al. 2007; Piconcelli et al. 2005; Zhou & Zhang 2010; Ponti et al. 2012; Gliozzi & Williams 2020).

Mrk 110 hosts a SMBH with a well-constrained mass value of $1.4 \pm 0.3 \times 10^8\ M_\odot$, measured from the detection of gravitationally redshifted emission in the variable component of all of the broad optical lines (Kollatschny 2003; Liu et al. 2017). Black hole (BH) mass values inferred for Mrk 110 from different, independent methods are in agreement with this value: optical spectro-polarimetric observations ($\log(M_{\rm BH}/M_\odot) = 8.32 \pm 0.21$; Afanasiev et al. 2019), X-ray excess variance ($\log(M_{\rm BH}/M_\odot) = 8.03^{+0.40}_{-0.30}$; Ponti et al. 2012), and X-ray scaling methods ($\log(M_{\rm BH}/M_\odot) = 8.2$–$8.5$; Williams et al. 2018). A much lower mass value using the virial method ($\sim 2 \times 10^7\ M_\odot$) has also been measured (Peterson et al. 2004). However, this latter method strongly depends on the inclination of the disc-like BLR system, contrary to the gravitational method. Indeed, as reported by Liu et al. (2017), the very large discrepancy between gravitational and virial masses can be explained by an adapted $f_{\rm FWHM}$ value of 8–16 for the virial measurement that depends on the disc-like BLR inclination. The commonly used value of $f_{\rm FWHM} \sim 1$ is relevant for an inclination angle of about 30 deg. This would imply a disc-like BLR system viewed almost face-on in Mrk 110 (Kollatschny 2003; Decarli et al. 2008; Liu et al. 2017).

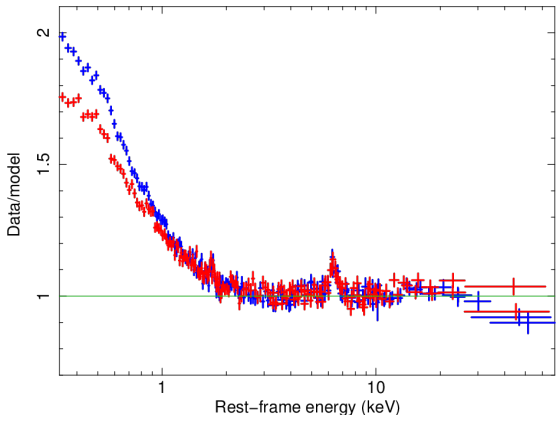

Fig. 1. Data-to-model ratio of the two simultaneous 2019 (blue) and 2020 (red) *XMM-Newton*-pn and *NuSTAR* spectra of Mrk 110 fit with a power-law model (with Galactic absorption) over the 3–5 and 7–10 keV energy ranges and then extrapolated over the whole energy range.

Mrk 110 was observed twice, simultaneously by *XMM-Newton* and *NuSTAR*, on November 16–17 2019 and April 5–6 2020 (Porquet et al. 2021; Reeves et al. 2021). The X-ray flux was a factor of ∼1.2 higher in the first observation compared to the second. From the long-term X-ray behaviour of Mrk 110 as observed by RXTE (Weng et al. 2020), the observations appear to be consistent with a moderately high state of the source. As shown in Fig. 1, the two X-ray broadband spectra (*XMM-Newton* pn and *NuSTAR*) are characterised by the presence of a prominent and absorption-free smooth soft X-ray excess, a weak Fe Kα line, and a lack of a strong Compton hump. Porquet et al. (2021) find for Mrk 110 (as for Ark 120 and TON S180) that relativistic reflection alone is not able to reproduce the soft X-ray excess and the hard X-ray spectral shape. Instead, a combination of soft (using COMPTT) and hard Comptonisation from a warm and hot corona, respectively, plus mild relativistic disc reflection is needed to reproduce the broadband X-ray continuum. Its inferred warm corona temperature, $kT_{\rm warm} \sim 0.3$ keV, is similar to the values found in other sub-Eddington AGNs (e.g., Gierliński & Done 2004; Porquet et al. 2004; Bianchi et al. 2009; Petrucci et al. 2018). Its hot corona temperature, $kT_{\rm hot} \sim 30$ keV (Porquet et al. 2021; Pal & Stalin 2023), is in the lower range of the average value measured from large samples of type-I radio-quiet AGNs (e.g., Middei et al. 2019; Panagiotou & Walter 2020; Akylas & Georgantopoulos 2021; Kamraj et al. 2022; Kang & Wang 2022).

The presence of a broad O VII soft X-ray emission line, first identified by Boller et al. (2007), was confirmed by the spectral analysis of the *XMM-Newton* resolution grating spectrometer (RGS) data obtained between 2004 and 2020 (Reeves et al. 2021). The O VII line flux varies significantly with the soft X-ray continuum flux level, being brightest when the continuum flux is highest (Reeves et al. 2021), similar to the reported behaviour of the optical He II line (Véron-Cetty et al. 2007). This O VII line originates from the accretion disc at a distance of a few tens of gravitational radii ($R_{\rm g} \equiv GM_{\rm BH}/c^2$). The inclination angle of the accretion disc has been well constrained ($9.9^{+1.0}_{-1.4}$ deg) from the spectral analysis of these O VII lines (Reeves et al. 2021). This is consistent with an almost face-on view of the disc-corona system, as also inferred for the disc-like BLR (Bian & Zhao 2002; Kollatschny 2003; Liu et al. 2017). In all the RGS spectra, no significant intrinsic X-ray warm absorption is present, with an upper limit for its column density of only 2.6×10^{20} cm^{-2},

Table 1. Observation log of the two simultaneous *XMM-Newton* and *NuSTAR* datasets.

Mission	Obs. ID	Obs. start (UTC)	Obs. end (UTC)	Exp. (ks) [(a)]	count s^{-1} [(b)]
NuSTAR	60502022002	2019 November 16 – 03:31:09	2019 November 18 – 00:56:09	86.8,86.2	0.64,0.62
XMM-Newton	0852590101	2019 November 17 – 09:02:57	2019 November 17 – 21:24:37	29.9	20.7
NuSTAR	60502022004	2020 April 5 – 14:26:09	2020 April 7 – 13:26:09	88.7,87.8	0.55,0.53
XMM-Newton	0852590201	2020 April 6 – 22:26:50	2020 April 7 – 11:55:10	32.7	16.2

Notes. [(a)]Net exposure time (livetime corrected from any background flaring period) for *XMM-Newton*-pn and *NuSTAR* (FPMA, FPMB). [(b)]Net source count rate over 0.3–10 keV for *XMM-Newton*-pn and over 3–79 keV for *NuSTAR* (FPMA, FPMB).

demonstrating that Mrk 110 is a bare AGN, irrespective of its flux level (Reeves et al. 2021). Mrk 110 is, therefore, an excellent target to probe its disc-corona system, which is viewed almost face-on and without any significant neutral or warm gas in its line of sight.

Following the first X-ray broadband spectral analysis of Mrk 110 using the two simultaneous 2019 and 2020 *XMM-Newton* and *NuSTAR* observations (Porquet et al. 2021), here we aim to probe the physical properties of its disc-corona system properties based on sophisticated models that were recently released to the community. As a first step, we use the recent X-ray REXCOR model (Xiang et al. 2022) to estimate the warm-corona heating fraction and then to confirm whether or not the soft X-ray excess can physically (mainly or at least partly) originate from a warm corona, as previously inferred using a more simplified modelling (Porquet et al. 2021). We then perform an in-depth SED analysis from UV to hard X-rays using the RELAGN model (Hagen & Done 2023a) – adding a relativistic reflection model (RELXILLCP; Dauser et al. 2013) – to infer the accretion rate and the physical properties of both the warm and hot corona. In Sect. 2, the data reduction and the analysis methods of the dataset are presented. The X-ray broadband analysis using the REXCOR model is performed in Sect. 3. In Sect. 4, the SED (from UV to hard X-rays) analysis using the RELAGN model complemented by relativistic reflection is reported. The main results are discussed in Sect. 5 and the conclusions are reported in Sect. 6.

2. Observations, data reduction, and analysis method

2.1. XMM-Newton and NuSTAR data reduction

The log of the simultaneous *XMM-Newton* and *NuSTAR* observations of Mrk 110 (*NuSTAR* cycle-5; PI: D. Porquet) used in this work is reported in Table 1. The *XMM-Newton*-EPIC (European Photon Imaging Camera) event files were reprocessed with the Science Analysis System (SAS; version 20.0.0), applying the latest calibration available on November 21, 2022. Due to the high source brightness, the EPIC-pn instrument was operated in the Small Window mode. We note that only the EPIC-pn (Strüder et al. 2001) data were used (selecting the event patterns 0–4, that is to say, single and double events) since they do not suffer from pile-up (contrary to the EPIC-MOS data; Turner et al. 2001) and have a much better sensitivity above ∼6 keV. The pn spectra were extracted from a circular region centred on Mrk 110, with a radius of 35″ to avoid the edge of the chip. The background spectra were extracted from a rectangular region in the lower part of the small window that contains no (or negligible) source photons. The total net exposure times, obtained after the correction for dead time and background flaring, are reported in Table 1. Redistribution matrix files (rmf) and ancillary response files (arf) were generated with the SAS tasks RMFGEN and ARFGEN, and were binned in order to over-sample the instrumental resolution by at least a factor of four, with no impact on the fit results. We notice that for the arf calculation, we applied the new option APPLYABSFLUXCORR=YES which allows for a correction of the order of 6–8% between 3 and 12 keV in order to reduce differences in the spectral shape between *XMM-Newton*-pn and *NuSTAR* spectra (Fürst 2022, XMM-CCF-REL-388, XMM-SOC-CAL-TN-0230)[1]. Finally, the background-corrected pn spectra were binned in order to have a signal-to-noise ratio greater than four in each spectral channel.

The UV data from the *XMM-Newton* Optical-UV Monitor (hereafter OM; Mason et al. 2001) were processed using the SAS script OMICHAIN. This script takes into account all necessary calibration processes (e.g., flat-fielding) and runs a source detection algorithm before performing aperture photometry (using an extraction radius of 5.″7) on each detected source, and combines the source lists from separate exposures into a single master list in order to compute mean corrected count rates. In order to take into account the OM calibration uncertainty of the conversion factor between the count rate and the flux, we quadratically added a representative systematic error of 1.5%[2] to the statistical error of the count rate, as done in Porquet et al. (2019) for the SED analysis of the bare AGN Ark 120.

NuSTAR (Harrison et al. 2013) observed Mrk 110 with its two co-aligned X-ray telescopes with corresponding Focal Plane Modules A (FPMA) and B (FPMB). The level 1 data products were processed with the *NuSTAR* Data Analysis Software (NuSTARDAS) package (v2.1.2, released on March 14 2022). Cleaned event files (level 2 data products) were produced and calibrated using standard filtering criteria with the NUPIPELINE task and the calibration files available in the *NuSTAR* calibration database (CALDB version: 20220829). Extraction radii for both the source and the background spectra were 60 arcsec. The corresponding net exposure time for the observations with the FPMA and FPMB are reported in Table 1. The processed rmf and arf files were provided on a linear grid of 40 eV steps. As the FWHM energy resolution of *NuSTAR* is 400 eV below ∼50 keV and increases to 1 keV at 86 keV (Harrison et al. 2013), we rebinned the rmf and arf files in energy and channel space by a factor of 4 to over-sample the instrumental energy resolution by at least a factor of 2.5. The background-corrected *NuSTAR* spectra were finally binned in order to have a signal-to-noise ratio greater than four in each spectral channel.

[1] https://xmmweb.esac.esa.int/docs/documents/CAL-SRN-0388-1-4.pdf
[2] https://xmmweb.esac.esa.int/docs/documents/CAL-SRN-0378-1-1.pdf

2.2. Spectral analysis method

The XSPEC v12.12.1 software package (Arnaud 1996) was used for the spectral analysis. As found by Reeves et al. (2021), there is no additional X-ray absorption compared to the Galactic value, which we fixed to 1.27×10^{20} cm^{-2} (HI4PI Collaboration 2016). We applied the X-ray absorption model TBNEW (VERSION 2.3.2) from Wilms et al. (2000), setting their interstellar medium (ISM) elemental abundances and using the cross-sections from Verner et al. (1996). We allowed for cross-calibration uncertainties between the two *NuSTAR* spectra and the *XMM-Newton*-pn spectra in the fit by including a cross-normalisation factor for the pair of *NuSTAR* FPMA and FPMB spectra, with respect to the pn spectra. We used χ^2 minimisation throughout, quoting errors with 90% confidence intervals for one interesting parameter ($\Delta\chi^2 = 2.71$). Default values of $H_0 = 67.66\,\mathrm{km\,s^{-1}\,Mpc^{-1}}$, $\Omega_\mathrm{m} = 0.3111$, and $\Omega_\Lambda = 0.6889$ were assumed (Planck Collaboration VI 2020).

3. X-ray simultaneous broadband spectral analysis with the ReXcor model: Probing the physical origin of the soft X-ray excess

REXCOR is a new phenomenological X-ray (0.3–100 keV) spectral fitting model of the disc-corona system in AGNs that self-consistently combines the effects of both the emission for a warm corona and ionised relativistic reflection (Xiang et al. 2022), which is based on the procedure described in Ballantyne (2020) and Ballantyne & Xiang (2020). The accretion energy released in the inner disc is apportioned between the three system components (Fig. 1 in Xiang et al. 2022): the warm corona, the hot corona (assuming a lamppost geometry, located above the spin axis of the black hole), and the accretion disc. This model includes the effects of relativistic light-bending and blurring up to $400\,R_\mathrm{g}$ using the RELCONV_LP convolution model (Dauser et al. 2013), assuming isotropic limb darkening. Depending on the fraction of energy dissipated in the warm and hot corona, as well as the warm corona heating fraction and optical depth, various soft X-ray excess shapes are produced (Figs. 4 and 5 in Xiang et al. 2022). The assumed metal abundances are from Morrison & McCammon (1983).

The eight publicly available table grid models are provided for two black hole spin values ($a = 0.90$ and $a = 0.99$), two hot-corona height values ($h = 5\,R_\mathrm{g}$ and $h = 20\,R_\mathrm{g}$), and two Eddington-ratio values ($\dot{m} = 0.1$ and $\dot{m} = 0.01$). These grids were computed for a disc inclination angle of 30 degrees. Therefore, in the present X-ray broadband analysis, we are not able to explore the impacts on the fit results using differing values. However, here our aim is primarily to estimate the contribution of a warm corona (compared to relativistic reflection) to the soft X-ray excess. The free model parameters of the REXCOR grids are: the hot-corona heating fraction with $0.02 \leq f_\mathrm{X} \leq 0.2$; the photon index of irradiating power law from the hot corona with $1.7 \leq \Gamma_\mathrm{hot} \leq 2.2$; the warm-corona heating fraction with $0.0 \leq h_\mathrm{f} \leq 0.8$: $h_\mathrm{f} = 0$ means that the soft X-ray excess is exclusively due to relativistic reflection; and the warm-corona Thomson depth with $10 \leq \tau_\mathrm{warm} \leq 30$.

The detailed fitting of the baseline model and the best-fit results for the four model grids are reported in Appendix A. The values of the warm-corona heating fraction are high ($h_\mathrm{f} \sim 50$–70%), indicating that the soft X-ray excess is mainly produced by a warm corona. This supports our previous results, obtained using a simplified Comptonisation model (COMPTT) plus relativistic reflection. We note that lower BH spin and/or larger coronal height values (which are not provided in the current model grids) would lead to a weaker reflection fraction (e.g., Dauser et al. 2014). This would then require a stronger contribution from the warm corona in order to reproduce the soft X-ray excess for Mrk 110. Therefore, the two BH spin values (and the two hot-corona-height values) investigated here could be considered as a conservative estimate of the warm corona contribution for Mrk 110. The warm-corona optical depth is rather high with $\tau_\mathrm{warm} \sim 13$–$28$. For both epochs, only a few percent of the accretion energy ($f_\mathrm{X} \sim 3$–7%) is dissipated in the lamppost hot corona.

The 0.3–10 keV flux ratios of the REXCOR and ZCUTOFFPL components strongly diverge from unity, with flux(REXCOR)/flux(ZCUTOFFPL) ~ 0.23. As discussed by Xiang et al. (2022), this could be due to effects not included in their models, such as, for example, a truncated accretion disc. This would lead to reduced emission from the warm corona and a reduction in the relativistic reflection fraction. Since the REXCOR model grids set the inner radius of the accretion disc to the inner stable circular orbit value (ISCO), we cannot perform the study assuming a truncated accretion disc. However, this truncated accretion disc scenario is investigated in the next section when modelling the spectral energy distribution (UV to hard X-rays) for both epochs with the RELAGN model.

4. SED analysis from UV to hard X-rays of Mrk 110 with the RELAGN model: Disc-corona system properties from its energetics

We now investigate the SED of Mrk 110 from UV to hard X-rays to determine the physical properties of its disc-corona system. For this purpose, we use the new RELAGN model, which is based on the AGNSED code of Kubota & Done (2018), but which incorporates general relativistic ray-tracing (Hagen & Done 2023a). The model consists of an inner optically-thin hot corona ($R_\mathrm{ISCO} \leq R \leq R_\mathrm{hot}$), a warm Comptonised disc ($R_\mathrm{hot} \leq R \leq R_\mathrm{warm}$) and an outer standard disc ($R_\mathrm{warm} \leq R \leq R_\mathrm{out}$). An illustration of this disc-corona geometry is displayed in Kubota & Done (2018, their Fig. 2). It is worth noting that for the RELAGN model the disc is truncated below R_hot; whereas for the REXCOR model (Sect. 3) the inner accretion disc radius is set to ISCO with a lamppost geometry for the hot corona. The model parameters of RELAGN are identical to those of AGNSED, except an additional parameter that allows for a colour–temperature correction[3] to the standard outer disc (f_col). For a detailed description of the RELAGN model we refer to Hagen & Done (2023a). We note that in the case where relativistic effects are not taken into account (AGNSED), the spin and accretion rate would be significantly underestimated for Mrk 110 (Table B.1), as also pointed out by Hagen & Done (2023b) for Fairall 9.

We only use data from the three shortest-wavelength UV filters with the OM (UVW2, UVM2, UVW1; effective wavelengths: 2120, 2310, 2910 Å, respectively) since the contaminations by the host galaxy and the close foreground star located at 5″.1-NE are negligible in these bands (Lobban et al., in prep.; hereafter L23). From monitoring over several months of Mrk 110 with *Neil Gehrels Swift* observatory the time delay between the X-rays and the UV emission is consistent with zero lag with an upper limit of ∼1 day (Vincentelli et al. 2021, L23). Moreover, the UV and X-rays fluxes are not observed to vary significantly above their statistical errors during the time-elapsed durations of the 2019 and 2020 *XMM-Newton* (∼8 h) and *NuSTAR* (∼1 day)

[3] In AGNSED, the colour–temperature correction is hardwired at unity.

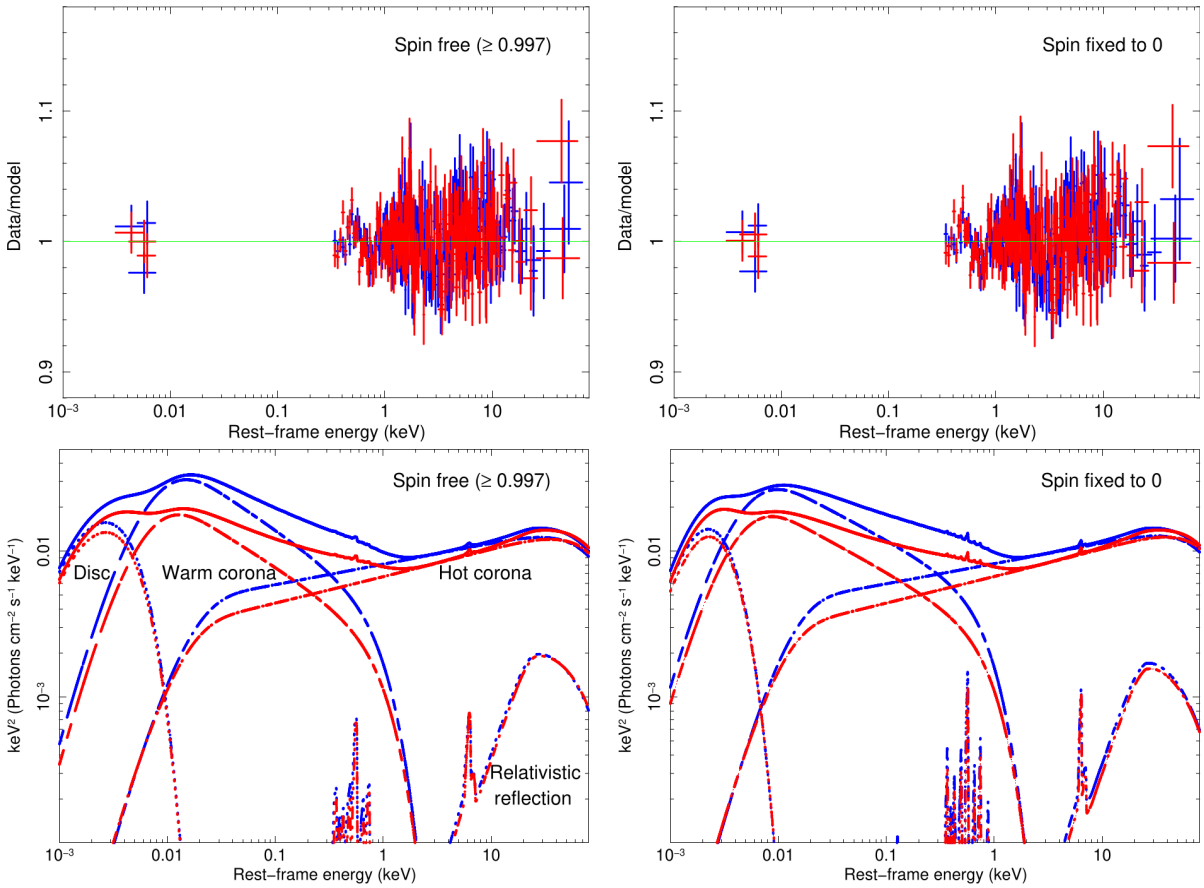

Fig. 2. SED fit from UV to hard X-rays of Mrk 110 using the RELAGN+RELXILLCP baseline model for the 2019 (blue) and 2020 (red) simultaneous *XMM-Newton* and *NuSTAR* spectra. Left panels: the black-hole spin is allowed to vary, and is found to be greater or equal to 0.997. The values of the best-fit parameters are reported in Table 2. Right panels: the black-hole spin value is fixed to zero. The best-fit parameter values are reported in Table 3. Top panels: data-to-model ratio. Bottom panels: intrinsic SED corrected for Galactic reddening and absorption (solid curves), with the main individual emission components of the baseline model: Outer disc (dotted curves), warm, optically-thick Comptonisation (dashed curves; warm corona), hot, optically-thin Comptonisation (dotted-dashed curves; hot corona), and relativistic reflection (three-dotted-dashed curves).

observations (L23). Therefore, the UV and X-ray emission can be considered to be effectively simultaneous on this timescale, which is an important assumption for the SED modelling.

The Galactic reddening of Mrk 110 is very low: $E(B-V) = 0.01$ (Schlafly & Finkbeiner 2011). For the colour-correction of the outer disc, we apply the relation in Done et al. (2012), by setting $f_{\rm col} < 0$ in the model. For each epoch, we tied the upper limit of the scale heights of the hot corona component to the $R_{\rm hot}$ value ($h_{\rm max}$ in $R_{\rm g}$), but we also checked that fixing it, for example, to 10 $R_{\rm g}$ does not impact our results. The distance of Mrk 110 is fixed to 155.7 Mpc (Wright 2006; Planck Collaboration VI 2020), its black hole mass is fixed to $1.4 \times 10^8\ M_{\odot}$ (Kollatschny 2003; Porquet et al. 2021), and its accretion disc inclination is fixed to 10 deg (Reeves et al. 2021).

Since a component of mild relativistic reflection is present (Reeves et al. 2021; Porquet et al. 2021) – but not included in the RELAGN model - we also added the RELXILLCP model, which uses an underlying Comptonisation continuum and a broken emissivity for the hot corona (Dauser et al. 2014, version 2.2). The emissivity indices were both fixed to the canonical values of three. Since the contribution of the relativistic reflection to the spectra is much weaker than that of RELAGN (Fig. 2, bottom panels), its real shape has no significant impact on the results. Indeed, similar results are found for the relativistic reflection component by assuming a lamppost geometry for the hot corona using RELXILLLPCP (Table B.1). The inner radius of the relativistic-reflection component was set to the $R_{\rm hot}$ radius since the disc is truncated below this value.

Our baseline model is: TBNEW×REDDEN(RELAGN + RELXILLCP + ZGAUSSIAN). As shown in Fig. 2 (top left panel), a very good fit from UV to hard X-rays is obtained with the physical parameters values reported in Table 2. Mrk 110 has a moderate accretion rate and its value (in log scale) decreases from $-1.03^{+0.01}_{-0.03}$ to $-1.14^{+0.01}_{-0.03}$ (at a 3.5σ confidence level), with the X-ray flux decreasing by only a factor of 1.13. The properties of the warm corona ($kT_{\rm warm}$ and $\Gamma_{\rm warm}$) are very similar between both epochs. There is a hint of a decrease of the mean value of $R_{\rm warm}$ when the source flux increases, though the values are compatible within their error bars calculated at 90% confidence level. For the hot corona, there is a slight spectral hardening and a decrease of the hot corona radius when the source flux increases (at a 2.8σ confidence level for both). This latter trend is similar to that found for the bare AGN Ark 120, which also accretes at a moderate Eddington rate (Porquet et al. 2018, 2019). The outer radius of the hot corona ($R_{\rm hot}$) is consistent with that found from the variability of the mildly-relativistic soft X-ray O VII lines (Reeves et al. 2021).

The best-fit spin value is found to be extreme with a lower limit of 0.997. However, we check whether different values of the spin can be really excluded by fixing it to values of 0, 0.5, 0.7, and 0.9. We fix the ionisation parameter (ξ; erg cm s^{-1}) of the accretion disc (in log scale) to unity in order to allow for

Table 2. Fits of the simultaneous 2019 and 2020 SED (UV to hard X-rays) of Mrk 110 with the RELAGN+RELXILLCP baseline model.

Parameter	2019 Nov.	2020 April
a	≥ 0.997	
$\log \dot{m}$	$-1.03^{+0.01}_{-0.03}$	$-1.14^{+0.01}_{-0.03}$
$kT_{\rm hot}$ (keV)	58^{+25}_{-8}	
$\Gamma_{\rm hot}$	1.86 ± 0.01	1.82 ± 0.01
$R_{\rm hot}$ ($R_{\rm g}$)	16^{+1}_{-4}	20 ± 1
$kT_{\rm warm}$ (keV)	0.23 ± 0.01	0.24 ± 0.01
$\Gamma_{\rm warm}$	$2.48^{+0.02}_{-0.03}$	$2.46^{+0.03}_{-0.04}$
$R_{\rm warm}$ ($R_{\rm g}$)	88^{+4}_{-3}	79^{+3}_{-8}
$\log \xi$	1.0 ± 0.2	
norm(relxillcp)	$2.1^{+0.6}_{-0.5} \times 10^{-5}$	$1.9^{+0.4}_{-0.5} \times 10^{-5}$
F(0.3–79 keV) [a]	11.8×10^{-11}	9.7×10^{-11}
L(0.3–79 keV) [b]	3.1×10^{44}	2.7×10^{44}
χ^2 (d.o.f.; $\chi^2_{\rm red}$)	1725.0 (1614; 1.07)	

Notes. [a]Observed fluxes (erg cm^{-2} s^{-1}). [b]Intrinsic luminosities (erg s^{-1}).

the presence of the O VII disc lines (Reeves et al. 2021). As shown in Table 3, the χ^2 value (d.o.f. = 1612) increases with the decrease of the spin value, by up to about $\Delta\chi^2 = +25$ for a zero-spin value. However, the fit is still satisfactory (Fig. 2: top right panel), indicating that even if the best-fit is found for a maximally-spinning black hole, a non-spinning black hole cannot be ruled out. For a black-hole spin value of 0, the accretion rate would decrease down to ~3–4%, while the radii of the hot and warm corona would increase by about a factor of two up to $\sim 50\,R_{\rm g}$ and $\sim 200\,R_{\rm g}$, respectively. Comparing the SED shape between a non-spinning black hole (Fig. 2: bottom-right panel) and a maximally-spinning black hole (Fig. 2: bottom-left panel), the emission of the warm corona is slightly weaker and is shifted to lower energies as expected from the increase of the outer hot corona radius, or in other words, to the increase of the inner warm-corona radius. This is due to the energy balance used in RELAGN. As the BH spin decreases, $R_{\rm hot}$ must increase in order to compensate for the smaller emitting area (due to in increase of the ISCO) and lower accretion efficiency. This in turn leads to a necessary increase in $R_{\rm warm}$, again to compensate for a smaller emitting area and lower efficiency. Readers can refer to Hagen & Done (2023a) for a detailed discussion.

5. Discussion

In previous work reported by Porquet et al. (2021), we have demonstrated that the first ever simultaneous *XMM-Newton* and *NuSTAR* spectrum of the bare AGN Mrk 110 – obtained in 2019 (November 16–17) and 2020 (April 5–6) – cannot be reproduced by purely relativistic reflection. From a simplified model combining soft and hard Comptonisation (using the COMPTT model) and mild relativistic reflection, the broadband X-ray continuum is very well reproduced. Therefore, in this work our first aim is to confirm with a more sophisticated model if the origin of the soft X-ray excess observed in Mrk 110 can physically originate from a warm corona. To test this, the REXCOR model is applied to the X-ray broadband spectra above 0.3 keV. This model self-consistently combines the effects of a warm corona with the X-ray relativistic reflection and allows for a physical estimate of the warm-corona heating fraction (Xiang et al. 2022). Then, we perform an in-depth SED analysis (from UV to hard X-rays) using the RELAGN model (Hagen & Done 2023a) – adding a relativistic reflection component – to infer the accretion rate and the physical properties of the disc-corona system. The main spectral analysis results are summarised and discussed below.

5.1. The warm corona as the main origin of the soft X-ray excess

The REXCOR model was applied to the 2019 and 2020 simultaneous X-ray broadband spectra of Mrk 110, noting the limitations of the range of paramer space available within the model grids (Sect. 3). For both epochs, the warm-corona heating fraction ($h_{\rm f}$) is large: ~50–70%, corroborating that the soft X-ray excess of Mrk 110 mainly originates from a warm corona rather than relativistic reflection (Porquet et al. 2021). The high values of the its optical depth ($\tau_{\rm warm} \sim$ 13–28) provide a smooth soft X-ray excess and are consistent with very recent modelling using a disc-corona structure, taking into account both magnetic and radiation pressure for an accretion rate of about 0.1 (Gronkiewicz et al. 2023).

Only a few percent of the accretion energy ($f_{\rm X}$ ~3–6%) is dissipated in the lamppost hot corona for Mrk 110, as also found by Xiang et al. (2022) for HE 1143−1820 and NGC 4593. Such a low value for $f_{\rm X}$ allows for a significant relative strength of the soft excess. Indeed, as discussed by Xiang et al. (2022), at such a value, the irradiated gas is less ionised, leading to significant absorption between about 1–4 keV (Fig. 2 in Ross et al. 1999), and then to a stronger observed contrast between the soft X-ray excess and the higher-energy emission. Our best-fit result would favour a spin value of 0.99 for Mrk 110, compared to the other available grids calculated with a black hole spin of 0.90. But, the model grids are only calculated for these two spin values (0.90 and 0.99) preventing us from investigating the results for other spin values for Mrk 110.

The low 0.3–10 keV fluxes of the REXCOR model – which only includes the emission and reflection component – compared to the primary continuum could suggest a truncated accretion disc, leading to weakened component of reflection emission. This truncated accretion disc scenario is further investigated when modelling the SED (UV to hard X-rays) of Mrk 110 for both epochs with the RELAGN model.

5.2. The properties of the disc-corona system of Mrk 110 inferred from its SED analysis

We analysed the 2019 and 2020 spectral energy distribution from UV to hard X-rays (Sect. 4), adopting the new model RELAGN based on the AGNSED model (Kubota & Done 2018), but including relativistic ray-tracing (Hagen & Done 2023a). The mild relativistic reflection is taken into account by adding the RELXILLCP model (Dauser et al. 2014).

This model reproduces the SED of Mrk 110 at both epochs very well (Fig. 2). The best-fit is found for an extreme black hole spin with a lower limit of 0.997. However, other spin values cannot be excluded. Indeed, for the case of a zero black hole spin, the fit is still statistically satisfactory. The outer radii of the hot and warm corona (depending on the black hole spin value) are located at a few 10s and $\sim 100\,R_{\rm g}$, respectively.

The measured Eddington rate range of Mrk 110 in 2019 and 2020 is about only 3–9% (depending on its flux level and the black hole spin), which is similar to that of the two BLS1 bare AGNs, Ark 120 (~3% in 2013 and ~7% in 2014; Porquet et al. 2019) and Fairall 9 (~10% in 2014; Hagen & Done 2023b). Though Mrk 110 exhibits a 10 keV X-ray flux (at both epochs)

Table 3. Simultaneous SED fits of the 2019 and 2020 simultaneous *XMM-Newton*-pn and *NuSTAR* spectra of Mrk 110.

Parameter	$a = 0$	$a = 0.5$	$a = 0.7$	$a = 0.90$	$a = 0.998$
			2019		
$\log \dot{m}$	-1.37 ± 0.01	-1.34 ± 0.01	-1.31 ± 0.01	-1.24 ± 0.01	-1.03 ± 0.01
$kT_{\rm hot}$ (keV)	42^{+17}_{-9}	43^{+17}_{-8}	44^{+18}_{-8}	46^{+22}_{-9}	57^{+29}_{-13}
$\Gamma_{\rm hot}$	1.86 ± 0.01	1.86 ± 0.01	1.86 ± 0.01	1.86 ± 0.01	1.86 ± 0.01
$R_{\rm hot}$ ($R_{\rm g}$)	43 ± 1	32 ± 1	27 ± 1	21 ± 1	16 ± 1
$kT_{\rm warm}$	0.20 ± 0.01	0.21 ± 0.01	0.21 ± 0.01	0.22 ± 0.01	0.23 ± 0.01
$\Gamma_{\rm warm}$	2.38 ± 0.01	2.41 ± 0.01	2.43 ± 0.02	2.45 ± 0.02	2.48 ± 0.03
$R_{\rm warm}$ ($R_{\rm g}$)	199^{+19}_{-15}	159^{+15}_{-12}	139^{+13}_{-11}	112^{+11}_{-10}	87 ± 9
$\log \xi$	1.0 (f)	1.0 (f)	1.0 (f)	1.0 (f)	1.0 (f)
Norm(relxill)	$1.9 \pm 0.5 \times 10^{-5}$	$1.9 \pm 0.5 \times 10^{-5}$	$2.0 \pm 0.5 \times 10^{-5}$	$2.1 \pm 0.5 \times 10^{-5}$	$2.2 \pm 0.6 \times 10^{-5}$
			2020		
$\log \dot{m}$	-1.46 ± 0.01	-1.43 ± 0.01	-1.40 ± 0.01	-1.34 ± 0.01	-1.14 ± 0.01
$kT_{\rm hot}$ (keV)	(t)	(t)	(t)	(t)	(t)
$\Gamma_{\rm hot}$	1.82 ± 0.01	1.82 ± 0.01	1.82 ± 0.01	1.82 ± 0.01	1.82 ± 0.01
$R_{\rm hot}$ ($R_{\rm g}$)	51^{+2}_{-1}	39 ± 1	33 ± 1	26 ± 1	20 ± 1
$kT_{\rm warm}$	0.22 ± 0.01	0.22 ± 0.01	0.23 ± 0.01	0.23 ± 0.01	0.24 ± 0.01
$\Gamma_{\rm warm}$	2.39 ± 0.01	2.41 ± 0.02	2.42 ± 0.02	$2.44^{+0.02}_{-0.03}$	2.46 ± 0.03
$R_{\rm warm}$ ($R_{\rm g}$)	179^{+15}_{-12}	144^{+11}_{-10}	126^{+10}_{-9}	101^{+9}_{-8}	79^{+8}_{-7}
$\log \xi$	(t)	(t)	(t)	(t)	(t)
norm(relxill)	$1.5 \pm 0.5 \times 10^{-5}$	$1.6 \pm 0.5 \times 10^{-5}$	$1.7 \pm 0.5 \times 10^{-5}$	$1.8 \pm 0.5 \times 10^{-5}$	$1.9 \pm 0.5 \times 10^{-5}$
χ^2/d.o.f.	1750.1/1612	1741.6/1612	1736.7/1612	1730.0/1612	1724.9/1612
$\chi^2_{\rm red}$	1.09	1.09	1.08	1.07	1.07

Notes. The model is: TBNEW(GAL)×REDDEN(GAL)(RELAGN+RELXILLCP+ZGAUSSIAN), fixing the black hole spin value. '(t)' means that the value has been tied between both epochs. '(f)' means that the values has been fixed.

similar to that observed for Ark 120 and Fairall 9, its UV peak emission is weaker by a factor of about 2–5 and 3–5 compared to these two latter objects, respectively (Porquet et al. 2019; Hagen & Done 2023b). In order to determine the physical origin(s) of such different SED shapes, a thorough comparison of their spectral and timing disc-corona properties and black hole spin is necessary. This is beyond the scope of this article and will be presented in a forthcoming work.

We found a trend of a hard X-ray spectral hardening and a decrease in the radius of the hot corona when the source flux increases, as found for the bare AGN Ark 120 (Porquet et al. 2019). The photon index of the hot corona of Mrk 110 displays a slight hardening between 2019 (highest X-ray flux) and 2020 (lowest X-ray flux). This is consistent with the 'softer-when-brighter' behaviour commonly observed in type-I AGNs with accretion rate above about 1% (e.g., Markowitz et al. 2003; Porquet et al. 2004; Younes et al. 2011; Soldi et al. 2014; Connolly et al. 2016; Ursini et al. 2016; Gliozzi et al. 2017; Weng et al. 2020). Importantly, the photon index values are found to be about 1.8–1.9, consistent with previous X-ray observations of Mrk 110 and, more generally, with BLS1s (e.g., Porquet et al. 2004; Zhou et al. 2010; Waddell & Gallo 2020; Gliozzi & Williams 2020).

As with any modelling, there are some possible caveats. The disc-corona geometry in AGNs is not established and could be different to that assumed by the RELAGN model. Additionally, a disc-like geometry is supposed when incorporating the relativistic ray-tracing, while the hot-corona geometry could have a much larger scale height, as found, for example, for the zero black-hole spin value where the maximum height of the corona is the highest (~40 $R_{\rm g}$). Therefore, we perform the SED spectral fit for a black-hole spin of zero, but fixing the maximum height of the corona height to 10 $R_{\rm g}$, rather than tying it to $R_{\rm hot}$ – however, no noticeable impact on the RELAGN parameter values is found.

In the SED analysis, the UV emission is supposed to come exclusively from the disc region – however, other contributions may be present. For example, in many AGNs, an excess in the U-band (around the Balmer jump at 3465 Å) continuum lags by about a factor of two – compared to an extrapolation of the trend through the rest of the UV-optical regime – is observed (Cackett et al. 2018, 2020; Edelson et al. 2019; Homayouni et al. 2022). This excess can be explained by the significant 'diffuse continuum' from the BLR itself or from the wind inwards of the BLR (Korista & Goad 2001, 2019; Lawther et al. 2018; Dehghanian et al. 2019; Mahmoud et al. 2023; Hagen & Done 2023a). Such a U-band continuum-lag excess is also observed in Mrk 110 when observed in relatively high-flux states (Vincentelli et al. 2022), but not at lower-flux states (Vincentelli et al. 2021), which are similar to the present 2019 and 2020 *XMM-Newton* and *NuSTAR* observations, respectively. Since the UVW1 filter band (which overlaps with the U band) includes the Balmer jump, the UV emission from the outer disc could be overestimated. Removing it from the SED fits only leads to a slight increase of the outer warm-corona radius (compatible with previous values within the error bars), and has a negligible impact on the other parameters.

5.3. The long-term variability of Mrk 110 combined with its low accretion rate: Indication for a (moderate) changing-state AGN ?

From the Sloan Digital Sky Survey (SDSS) and Pan-STARRS1 (MacLeod et al. 2016), about 1% of their AGN sample display variability amplitude in the g band of at least one magnitude on

time-scales shorter than 15 years, and up to 30–50% on longer time-scales (see also MacLeod et al. 2019; López-Navas et al. 2022; Hon et al. 2022; Temple et al. 2023b). These types of AGNs, which could be a non-negligible fraction of the overall AGN population, have been named 'changing-look' (CL) AGNs. They can experience rapid apparent changes in states, from a type 1 AGN with strong, broad emission lines to a type 2 AGN with only narrow emission lines (no more BLR) – or, conversely. This phenomenon can be explained, for example, by a significant change in the accretion rate (in this case, these AGNs are also called 'changing-state' AGNs), or in some cases simply by transient obscuration of the BLR. Changing-state behaviour can occur on timescales of only a few years, typically much faster than the viscous timescale from standard accretion theory. Changing-state AGNs exhibit lower Eddington ratios relative to the less variable AGN population (MacLeod et al. 2016; Green et al. 2022).

Interestingly, Mrk 110 is known to be a strongly variable source. In particular, its optical lines and continuum are highly variable (e.g., Bischoff & Kollatschny 1999; Kollatschny et al. 2001; Véron-Cetty et al. 2007; Vincentelli et al. 2021, 2022; Homan et al. 2023). As found from the very long-term (∼30 years; 1987–2019) optical behaviour of Mrk 110 (Homan et al. 2023), the He II λ4686 emission line – used as a proxy of the unobservable FUV continuum – displays dramatic variability of a factor of forty and is much higher than the optical continuum. Also shown in Fig. 2 from Homan et al. (2023), a very significant drop of the Hβ line flux occured within a very short duration of ∼3–4 years with the lowest state observed in December 2001. Variable obscuration by intervening dust as the origin of the variability has been ruled out (Homan et al. 2023), meaning that the variability of Mrk 110 is intrinsic to its disc-corona system. Moreover, the low Eddington ratio measured for Mrk 110 is also consistent with what is observed for changing-state AGNs, and could explain its relatively steep Balmer decrement of Hα/Hβ (∼4; Jaffarian & Gaskell 2020). Indeed, as shown in the recent work by Wu et al. (2023) – based on a photoionisation modelling using the Cloudy code (Ferland et al. 2017) taking into account the SED distribution change shapes at different accretion rates – there is a strong negative correlation between Hα/Hβ and Eddington ratio is found (see also, La Mura et al. 2007; Lu et al. 2019).

During the lowest optical state in December 2001 with SDSS, the broad component of the He II line vanished, while the broad components of Hα, Hβ and He I λ5876 Å – though much weaker and narrower – are still present (Homan et al. 2023). Since some part of the BLR is still detected, Mrk 110 did not switch to a Seyfert type 2, but during its lowest optical state could be classified as an intermediate Seyfert type. Unfortunately, no X-ray data are available during this lowest optical state. The closest-in-time X-ray observation of Mrk 110 was obtained with *Beppo*SAX in April 2001 where the source was observed in a lower 2–10 keV flux state (∼ a factor of three) compared to two preceeding *Beppo*SAX observations made in May and November 2000 (Deluit & Courvoisier 2003; Dadina 2007), which have similar X-ray fluxes to the present 2019 and 2020 *XMM-Newton* observations. Since the April 2001 X-ray observation of Mrk 110 occured a few months before its optical lowest flux state, no contemporaneous information within the lag timescale of Hβ (∼25–30 days; Peterson et al. 2004) is available to establish if the source was also in a very low X-ray flux state. Contemporaneous or simultaneous multi-wavelength data are crucial, since as shown from the long-term X-ray light curves (2000–2012) obtained with RXTE, Mrk 110 exhibits significant X-ray flux variations with a flux amplitude of up to about 5 over month-timescales.

Therefore, combining its multi-wavelength spectral and timing characteristics, and the low Eddington ratio inferred from this work, Mrk 110 could be classified as a (moderate) changing-state AGN. To confirm this scenario, further simultanous or contemporaneous optical-UV-X-rays spectral and timing monitoring of Mrk 110 at very different flux levels are necessary, especially during its lowest state.

6. Conclusion

Very high signal-to-noise broadband data of bare AGNs are the key to probing the disc-corona system and, in particular, to probing hybrid models combining both soft-hard Comptonisation (warm-hot corona) and relativistic reflection emission. Here, we applied two brand new codes allowing us to physically take into account the presence of a warm corona, REXCOR and RELAGN, for the X-ray-bright bare AGN Mrk 110. Its simultaneous broadband *XMM-Newton* and *NuSTAR* X-ray spectra in 2019 and 2020 are satisfactorily reproduced by the REXCOR model. The high values of the warm-corona heating confirm that the soft X-ray excess of Mrk 110 – for both epochs – originates mainly from a warm corona rather than relativistic reflection (Porquet et al. 2021). Using the RELAGN model, its UV to hard X-ray SEDs are very well reproduced by the warm- and hot-corona components plus mild relativistic reflection. From the best-fit model with a maximally-rotating SMBH (though other spin values cannot be definitively excluded on a simple statistical basis), the radius of the hot corona is a few 10s R_g, while the warm corona then extends up to ∼100 R_g. For both epochs, the relative strength of the UV compared to X-rays is rather weak, compared to the two other bright bare AGNs Ark 120 and Fairall 9, which display similar X-ray fluxes. The SED analysis of Mrk 110 shows that its disc-corona system has a low-to-moderate Eddington ratio of about a few percent. Combined with its long-term optical properties, Mrk 110 could be classified as a moderate changing-state AGN.

The success of both the REXCOR and RELAGN models in fitting the X-ray spectrum and broadband SED of Mrk 110 is really promising for such disc-corona scenarios including the presence of a warm corona. This provides additional strong evidence that the disc-corona system in AGNs can be more complex than the usual scenario assuming purely relativistic reflection from a hot corona with a lamppost geometry onto a standard accretion disc. This reinforces the importance of considering AGN disc-corona systems departing from the standard accretion disc theory (e.g., Mitchell et al. 2023; Temple et al. 2023a; Hagen & Done 2023b) and to continue developing and improving self-consistent models incorporating both hot-warm corona and relativistic reflection. The growing number of highly variable AGNs (over time-scales of a few years) which are similar to Mrk 110 challenges the standard accretion theory and demonstrates the importance of long-term simultaneous or contemporaneous multi-wavelength monitoring on both single targets and large AGN surveys (e.g., Green et al. 2022; Kovačević et al. 2022; Kynoch et al. 2023; Temple et al. 2023b).

Acknowledgements. We thank the referee for a constructive review of our work that contributed to improve our paper. The paper is based on observations obtained with the *XMM-Newton* ESA science mission with instruments and contributions directly funded by ESA member states and the USA (NASA). This work made use of data from the *NuSTAR* mission, a project led by the California Institute of Technology, managed by the Jet Propulsion Laboratory,

and funded by NASA. This research has made use of the *NuSTAR* Data Analysis Software (NuSTARDAS) jointly developed by the ASI Science Data Center and the California Institute of Technology. This research has made use of NASA's Astrophysics Data System. This research has made use of the SIMBAD database, operated at CDS, Strasbourg, France. This research has made use of the NASA/IPAC Extragalactic Database (NED) which is operated by the California Institute of Technology, under contract with the National Aeronautics and Space Administration. This work was supported by the French space agency (CNES). This research has made use of computing facilities operated by CeSAM data centre at LAM, Marseille, France. S.H. acknowledges support from the Science and Technology Facilities Council (STFC) through the studentship ST/V506643/1. C.D. acknowledges support from STFC through grant ST/T000244/1.

References

Adams, T. F. 1977, ApJS, 33, 19
Afanasiev, V. L., Popović, L. Č., & Shapovalova, A. I. 2019, MNRAS, 482, 4985
Akylas, A., & Georgantopoulos, I. 2021, A&A, 655, A60
Arnaud, K. A. 1996, ASP Conf. Ser., 101, 17
Ballantyne, D. R. 2020, MNRAS, 491, 3553
Ballantyne, D. R., & Xiang, X. 2020, MNRAS, 496, 4255
Bian, W., & Zhao, Y. 2002, A&A, 395, 465
Bianchi, S., Guainazzi, M., Matt, G., Fonseca Bonilla, N., & Ponti, G. 2009, A&A, 495, 421
Bischoff, K., & Kollatschny, W. 1999, A&A, 345, 49
Boller, T., Balestra, I., & Kollatschny, W. 2007, A&A, 465, 87
Boroson, T. A., & Green, R. F. 1992, ApJS, 80, 109
Cackett, E. M., Chiang, C.-Y., McHardy, I., et al. 2018, ApJ, 857, 53
Cackett, E. M., Gelbord, J., Li, Y.-R., et al. 2020, ApJ, 896, 1
Chen, S., Laor, A., & Behar, E. 2022, MNRAS, 515, 1723
Connolly, S. D., McHardy, I. M., Skipper, C. J., & Emmanoulopoulos, D. 2016, MNRAS, 459, 3963
Crenshaw, D. M. 1986, ApJS, 62, 821
Crummy, J., Fabian, A. C., Gallo, L., & Ross, R. R. 2006, MNRAS, 365, 1067
Dadina, M. 2007, A&A, 461, 1209
Dauser, T., Garcia, J., Wilms, J., et al. 2013, MNRAS, 430, 1694
Dauser, T., García, J., Parker, M. L., Fabian, A. C., & Wilms, J. 2014, MNRAS, 444, L100
Decarli, R., Dotti, M., Fontana, M., & Haardt, F. 2008, MNRAS, 386, L15
Dehghanian, M., Ferland, G. J., Peterson, B. M., et al. 2019, ApJ, 882, L30
Deluit, S., & Courvoisier, T. J. L. 2003, A&A, 399, 77
Done, C., Davis, S. W., Jin, C., Blaes, O., & Ward, M. 2012, MNRAS, 420, 1848
Edelson, R., Gelbord, J., Cackett, E., et al. 2019, ApJ, 870, 123
Fabian, A. C., Zoghbi, A., Wilkins, D., et al. 2012, MNRAS, 419, 116
Ferland, G. J., Chatzikos, M., Guzmán, F., et al. 2017, Rev. Mex. Astron. Astrofis., 53, 385
Gierliński, M., & Done, C. 2004, MNRAS, 349, L7
Gliozzi, M., & Williams, J. K. 2020, MNRAS, 491, 532
Gliozzi, M., Papadakis, I. E., Grupe, D., Brinkmann, W. P., & Räth, C. 2017, MNRAS, 464, 3955
Green, P. J., Pulgarin-Duque, L., Anderson, S. F., et al. 2022, ApJ, 933, 180
Gronkiewicz, D., Różańska, A., Petrucci, P.-O., & Belmont, R. 2023, A&A, 675, A198
Grupe, D., Wills, B. J., Leighly, K. M., & Meusinger, H. 2004, AJ, 127, 156
Hagen, S., & Done, C. 2023a, MNRAS, 525, 3455
Hagen, S., & Done, C. 2023b, MNRAS, 521, 251
Harrison, F. A., Craig, W. W., Christensen, F. E., et al. 2013, ApJ, 770, 103
HI4PI Collaboration (Ben Bekhti, N., et al.) 2016, A&A, 594, A116
Homan, D., Lawrence, A., Ward, M., et al. 2023, MNRAS, 519, 1745
Homayouni, Y., Sturm, M. R., Trump, J. R., et al. 2022, ApJ, 926, 225
Hon, W. J., Wolf, C., Onken, C. A., Webster, R., & Auchettl, K. 2022, MNRAS, 511, 54
Hutchings, J. B., & Craven, S. E. 1988, AJ, 95, 677
Jaffarian, G. W., & Gaskell, C. M. 2020, MNRAS, 493, 930
Järvelä, E., Dahale, R., Crepaldi, L., et al. 2022, A&A, 658, A12
Kamraj, N., Brightman, M., Harrison, F. A., et al. 2022, ApJ, 927, 42
Kang, J.-L., & Wang, J.-X. 2022, ApJ, 929, 141
Kollatschny, W. 2003, A&A, 412, L61
Kollatschny, W., Bischoff, K., Robinson, E. L., Welsh, W. F., & Hill, G. J. 2001, A&A, 379, 125
Korista, K. T., & Goad, M. R. 2001, ApJ, 553, 695
Korista, K. T., & Goad, M. R. 2019, MNRAS, 489, 5284
Kovačević, A. B., Radović, V., Ilić, D., et al. 2022, ApJS, 262, 49
Kubota, A., & Done, C. 2018, MNRAS, 480, 1247
Kukula, M. J., Dunlop, J. S., Hughes, D. H., & Rawlings, S. 1998, MNRAS, 297, 366
Kynoch, D., Mitchell, J. A. J., Ward, M. J., et al. 2023, MNRAS, 520, 2781
Laha, S., Guainazzi, M., Dewangan, G. C., Chakravorty, S., & Kembhavi, A. K. 2014, MNRAS, 441, 2613
La Mura, G., Popović, L. Č., Ciroi, S., Rafanelli, P., & Ilić, D. 2007, ApJ, 671, 104
Lawther, D., Goad, M. R., Korista, K. T., Ulrich, O., & Vestergaard, M. 2018, MNRAS, 481, 533
Liu, H. T., Feng, H. C., & Bai, J. M. 2017, MNRAS, 466, 3323
López-Navas, E., Martínez-Aldama, M. L., Bernal, S., et al. 2022, MNRAS, 513, L57
Lu, K.-X., Zhao, Y., Bai, J.-M., & Fan, X.-L. 2019, MNRAS, 483, 1722
MacKenty, J. W. 1990, ApJS, 72, 231
MacLeod, C. L., Ross, N. P., Lawrence, A., et al. 2016, MNRAS, 457, 389
MacLeod, C. L., Green, P. J., Anderson, S. F., et al. 2019, ApJ, 874, 8
Magdziarz, P., Blaes, O. M., Zdziarski, A. A., Johnson, W. N., & Smith, D. A. 1998, MNRAS, 301, 179
Mahmoud, R. D., Done, C., Porquet, D., & Lobban, A. 2023, MNRAS, 521, 3585
Markowitz, A., & Edelson, R. 2004, ApJ, 617, 939
Markowitz, A., Edelson, R., & Vaughan, S. 2003, ApJ, 598, 935
Mason, K. O., Breeveld, A., Much, R., et al. 2001, A&A, 365, L36
Matt, G., Marinucci, A., Guainazzi, M., et al. 2014, MNRAS, 439, 3016
Matzeu, G. A., Nardini, E., Parker, M. L., et al. 2020, MNRAS, 497, 2352
Middei, R., Bianchi, S., Petrucci, P. O., et al. 2019, MNRAS, 483, 4695
Miller, P., Rawlings, S., & Saunders, R. 1993, MNRAS, 263, 425
Mitchell, J. A. J., Done, C., Ward, M. J., et al. 2023, MNRAS, 524, 1796
Morrison, R., & McCammon, D. 1983, ApJ, 270, 119
Osterbrock, D. E. 1977, ApJ, 215, 733
Pal, I., & Stalin, C. S. 2023, MNRAS, 518, 2529
Panagiotou, C., & Walter, R. 2020, A&A, 640, A31
Panessa, F., Pérez-Torres, M., Hernández-García, L., et al. 2022, MNRAS, 510, 718
Peterson, B. M., Foltz, C. B., Cranshaw, D. M., Meyers, K. A., & Byard, P. L. 1984, ApJ, 279, 529
Peterson, B. M., Wanders, I., Bertram, R., et al. 1998, ApJ, 501, 82
Peterson, B. M., Ferrarese, L., Gilbert, K. M., et al. 2004, ApJ, 613, 682
Petrucci, P.-O., Ursini, F., De Rosa, A., et al. 2018, A&A, 611, A59
Piconcelli, E., Jimenez-Bailón, E., Guainazzi, M., et al. 2005, A&A, 432, 15
Planck Collaboration VI. 2020, A&A, 641, A6
Ponti, G., Papadakis, I., Bianchi, S., et al. 2012, A&A, 542, A83
Porquet, D., Reeves, J. N., O'Brien, P., & Brinkmann, W. 2004, A&A, 422, 85
Porquet, D., Dubau, J., & Grosso, N. 2010, Space. Sci. Rev., 157, 103
Porquet, D., Reeves, J. N., Matt, G., et al. 2018, A&A, 609, A42
Porquet, D., Done, C., Reeves, J. N., et al. 2019, A&A, 623, A11
Porquet, D., Reeves, J. N., Grosso, N., Braito, V., & Lobban, A. 2021, A&A, 654, A89
Reeves, J. N., Porquet, D., Braito, V., Grosso, N., & Lobban, A. 2021, A&A, 649, L3
Ross, R. R., Fabian, A. C., & Young, A. J. 1999, MNRAS, 306, 461
Schlafly, E. F., & Finkbeiner, D. P. 2011, ApJ, 737, 103
Soldi, S., Beckmann, V., Baumgartner, W. H., et al. 2014, A&A, 563, A57
Strüder, L., Briel, U., Dennerl, K., et al. 2001, A&A, 365, L18
Temple, M. J., Matthews, J. H., Hewett, P. C., et al. 2023a, MNRAS, 523, 646
Temple, M. J., Ricci, C., Koss, M. J., et al. 2023b, MNRAS, 518, 2938
Tombesi, F., Cappi, M., Reeves, J. N., et al. 2013, MNRAS, 430, 1102
Turner, M. J. L., Abbey, A., Arnaud, M., et al. 2001, A&A, 365, L27
Ursini, F., Petrucci, P.-O., Matt, G., et al. 2016, MNRAS, 463, 382
Verner, D. A., Ferland, G. J., Korista, K. T., & Yakovlev, D. G. 1996, ApJ, 465, 487
Véron-Cetty, M. P., Véron, P., Joly, M., & Kollatschny, W. 2007, A&A, 475, 487
Vestergaard, M. 2002, ApJ, 571, 733
Vincentelli, F. M., McHardy, I., Cackett, E. M., et al. 2021, MNRAS, 504, 4337
Vincentelli, F. M., McHardy, I., Hernández Santisteban, J. V., et al. 2022, MNRAS, 512, L33
Waddell, S. G. H., & Gallo, L. C. 2020, MNRAS, 498, 5207
Wehinger, P. A., & Wyckoff, S. 1977, MNRAS, 181, 211
Weng, S.-S., Chen, Y., Wang, T.-T., et al. 2020, MNRAS, 491, 2576
Williams, J. K., Gliozzi, M., & Rudzinsky, R. V. 2018, MNRAS, 480, 96
Wilms, J., Allen, A., & McCray, R. 2000, ApJ, 542, 914
Woo, J.-H., & Urry, C. M. 2002, ApJ, 579, 530
Wright, E. L. 2006, PASP, 118, 1711
Wu, J., Wu, Q., Xue, H., Lei, W., & Lyu, B. 2023, ApJ, 950, 106
Xiang, X., Ballantyne, D. R., Bianchi, S., et al. 2022, MNRAS, 515, 353
Xu, C., Livio, M., & Baum, S. 1999, AJ, 118, 1169
Younes, G., Porquet, D., Sabra, B., & Reeves, J. N. 2011, A&A, 530, A149
Zhou, X.-L., & Zhang, S.-N. 2010, ApJ, 713, L11
Zhou, X.-L., Zhang, S.-N., Wang, D.-X., & Zhu, L. 2010, ApJ, 710, 16

Appendix A: Additional information about the X-ray broadband fits using the REXCOR model

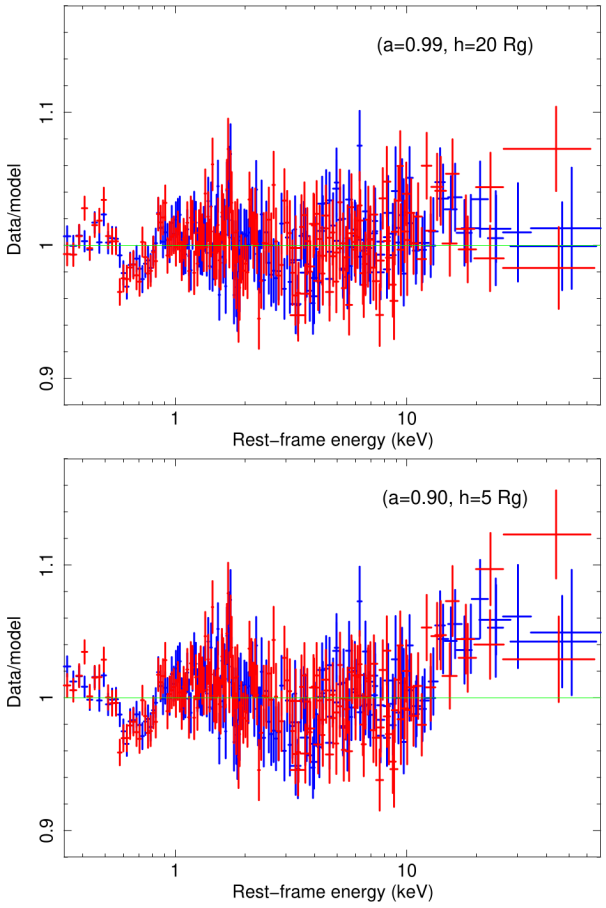

Fig. A.1. Data-to-model ratio of the fits using the REXCOR model grids for the 2019 (blue) and 2020 (red) simultaneous *XMM-Newton* and *NuSTAR* spectra. The inferred parameter values are reported in Table A.1. Top panel: model calculated for a spin of 0.99 and a hot corona height of 20 R_g (χ^2/d.o.f.=1777/1605). Bottom panel: model calculated for a spin of 0.90 and a hot corona height of 5 R_g (χ^2/d.o.f.=1921/1605).

Table A.1. Best-fit results of the two simultaneous 2019 and 2020 X-ray broadband spectra (*XMM-Newton* and *NuSTAR*) with a model of the form: TBNEW(GAL)×(REXCOR + ZCUTOFFPL + ZGAUSSIAN).

parameter	2019 Nov	2020 April
(a=0.99, h=5)		
f_X	$4.4^{+0.6}_{-0.5}\times10^{-2}$	$4.6^{+0.8}_{-0.6}\times10^{-2}$
$\Gamma_{\rm hot}$	1.78±0.01	1.73±0.01
h_f	$0.48^{+0.01}_{-0.02}$	$0.48^{+0.02}_{-0.04}$
$\tau_{\rm warm}$	$14.7^{+0.3}_{-1.5}$	$13.0^{+0.6}_{-1.1}$
log F(reXcor)$^{(a)}$	−10.94±0.01	$-11.10^{+0.01}_{-0.02}$
log F(zcutoffpl)$^{(a)}$	−10.33±0.01	−10.41±0.01
χ^2/d.o.f. ($\chi^2_{\rm red}$)	1815.9/1605 (1.13)	
(a=0.99, h=20)		
f_X	$3.2^{+1.2}_{-0.6}\times10^{-2}$	$3.7^{+1.1}_{-0.7}\times10^{-2}$
$\Gamma_{\rm hot}$	1.79±0.01	1.75±0.01
h_f	$0.50^{+0.03}_{-0.06}$	$0.52^{+0.02}_{-0.05}$
$\tau_{\rm warm}$	15.5±1.5	$15.4^{+2.2}_{-1.0}$
log F(reXcor)$^{(a)}$	−10.96±0.02	$-11.14^{+0.02}_{-0.03}$
log F(zcutoffpl)$^{(a)}$	−10.33±0.01	−10.40±0.01
χ^2/d.o.f. ($\chi^2_{\rm red}$)	1777.3/1605 (1.11)	
(a=0.90, h=5)		
f_X	$6.0^{+2.4}_{-1.2}\times10^{-2}$	$6.3^{+1.1}_{-0.9}\times10^{-2}$
$\Gamma_{\rm hot}$	1.79±0.01	1.74±0.01
h_f	$0.62^{+0.01}_{-0.02}$	$0.62^{+0.02}_{-0.01}$
$\tau_{\rm warm}$	$20.9^{+1.9}_{-2.7}$	$19.3^{+0.6}_{-0.7}$
log F(reXcor)$^{(a)}$	−10.98±0.01	−11.15±0.01
log F(zcutoffpl)$^{(a)}$	−10.33±0.01	−10.39±0.01
χ^2/d.o.f. ($\chi^2_{\rm red}$)	1921.3/1605 (1.20)	
(a=0.90, h=20)		
f_X	$4.0^{+2.6}_{-1.2}\times10^{-2}$	$5.5^{+0.9}_{-1.3}\times10^{-2}$
$\Gamma_{\rm hot}$	1.81±0.01	1.78±0.01
h_f	$0.63^{+0.05}_{-0.02}$	0.72±0.02
$\tau_{\rm warm}$	$21.1^{+4.8}_{-1.1}$	$27.6^{+1.5}_{-0.8}$
log F(reXcor)$^{(a)}$	−11.00±0.01	−11.23±0.01
log F(zcutoffpl)$^{(a)}$	−10.32±0.01	−10.39±0.01
χ^2/d.o.f. ($\chi^2_{\rm red}$)	1834.0/1605 (1.14)	

Note. $^{(a)}$ 0.3–10 keV pn unabsorbed fluxes (erg cm^{-2} s^{-1}).

The REXCOR grid models do not include the underlying hard X-ray power-law continuum, therefore we also added a cut-off power-law component by using ZCUTOFFPL (Xiang et al. 2022). The high-energy cut-off values were fixed to the mean values found in Porquet et al. (2021) when fitting the data above 3 keV with ZCUTOFFPL: 187 keV in 2019 and 216 keV. The weak Fe Kα narrow core (EW ∼40 eV, Porquet et al. 2021) was taken into account by including a Gaussian emission line (σ=10 eV) at 6.4 keV. We applied the model grids calculated for an Eddington ratio of 0.1. The baseline model is: TBNEW(GAL)×(REXCOR+ZCUTOFFPL+ZGAUSSIAN). The 2019 and 2020 *XMM-Newton* and *NuSTAR* spectra were fit simultaneously with $h_{\rm f}$, Γ, $f_{\rm h}$, and $\tau_{\rm T}$ free to vary between the two epochs. For each epoch, the photon index of REXCOR and ZCUTOFFPL were tied together.

Statistically speaking, the best-fit result is found for the model grid calculated for a spin value of 0.99 and a lamppost height of 20 $R_{\rm g}$ (Table A.1 and Fig. A.1: top panel). As shown in Fig. A.1 (bottom panel), the data-model ratio for a=0.90 and h=5 $R_{\rm g}$, which corresponds to the highest χ^2 value, shows some noticeable deviation in the hard X-ray range. In all fits, there are small negative deviations of the data-model ratio of about 3% at ∼0.5–0.6 keV, which is in the energy range of the O VII triplet lines. As pointed out by Xiang et al. (2022), the sensitivity to temperature, density and optical depth of the He-like triplets (Porquet et al. 2010) are not correctly described by the REXCOR model and could lead to residual of a few percent. This slight discrepancy could also be due to the disc inclination of 30 degrees assumed when building the REXCOR grids, leading to slightly larger line widths than for a system viewed almost face on; and/or to the oxygen abundance that could potentially be a bit overestimated, leading to an increase in the model of the O VII line flux.

Appendix B: Different SED models for the 2019 and 2020 simultaneous *XMM-Newton* and *NuSTAR* observations

In Table B.1, we report the best-fit values found for different SED models for comparison purposes:

- RELAGN+RELXILLCP: same baseline as reported in §4 (Table 2): RELAGN+RELXILLCP+ZGAUSSIAN;
- RELAGN+RELXILLLPCP: same as the baseline model, except that a relativistic model assuming a lamppost geometry was used;
- RELAGN: no relativistic reflection component was included;
- AGNSED+RELXILLCP: the AGNSED model was used instead of RELAGN, that is to say no general relativistic ray-tracing included;
- AGNSED: same as the fourth row except that no relativistic reflection component was included.

The comparison of the best-fit values shows that similar results are found for RELAGN+RELXILLCP and RELAGN+RELXILLLPCP. Indeed, for Mrk 110, the relativistic contribution is found to be weak (Porquet et al. 2021), and so its exact modelling impact is negligible here. However, for the RELAGN solo fit, the best-fit value is higher and the spin value is less contrained with a smaller lower limit leading to slightly higher $R_{\rm hot}$ and $R_{\rm warm}$ values (for a comparable $\dot{m}$ value). Comparing RELAGN+RELXILLCP and AGNSED+RELXILLCP, we find that the values of $\dot{m}$ and spin are significantly underestimated when the relativistic effects are not included. This confirmed the behaviour found by Hagen & Done (2023b) for Fairall 9, indeed, the 'increase in Eddington ratio and spin is compensating for the reduction in observed power from the general relativistic ray-tracing'.

Table B.1. Simultaneous SED fits to the 2019 and 2020 simultaneous *XMM-Newton*-pn and *NuSTAR* spectra of Mrk 110.

parameter	RELAGN + RELXILLCP	RELAGN + RELXILLLPCP	RELAGN	AGNSED + RELXILLCP	AGNSED
			2019		
a	≥0.997	≥0.996	≥0.82	$0.84^{+0.03}_{-0.17}$	$0.81^{+0.11}_{-0.23}$
$\log \dot{m}$	$-1.03^{+0.01}_{-0.03}$	$-1.04^{+0.01}_{-0.03}$	$-1.06^{+0.06}_{-0.19}$	−1.49±0.01	−1.46±0.02
$kT_{\rm hot}$ (keV)	58^{+25}_{-8}	55^{+24}_{-6}	≥76	34^{+10}_{-6}	47^{+71}_{-15}
$\Gamma_{\rm hot}$	1.86±0.01	1.86±0.01	1.83±0.01	1.86±0.01	1.83±0.01
$R_{\rm hot}$ ($R_{\rm g}$)	16^{+1}_{-4}	16^{+1}_{-5}	18^{+1}_{-2}	14^{+5}_{-3}	15^{+7}_{-4}
$kT_{\rm warm}$	0.23±0.01	0.23±0.01	0.23±0.01	0.22±0.01	0.22±0.01
$\Gamma_{\rm warm}$	$2.48^{+0.02}_{-0.03}$	$2.48^{+0.02}_{-0.03}$	$2.45^{+0.02}_{-0.03}$	2.50±0.04	$2.47^{+0.04}_{-0.02}$
$R_{\rm warm}$ ($R_{\rm g}$)	88^{+4}_{-3}	87^{+3}_{-7}	98^{+12}_{-9}	73^{+29}_{-21}	81^{+36}_{-28}
$\log \xi$	1.0±0.2	$1.0^{+0.1}_{-0.2}$	–	$1.0^{+0.2}_{-0.1}$	–
norm(relxill)	$1.1\pm0.2\times10^{-5}$	$3.6^{+0.8}_{-0.4}\times10^{-5}$	–	$2.0\pm0.5\times10^{-5}$	–
			2020		
a	(t)	(t)	(t)	(t)	(t)
$\log \dot{m}$	$-1.14^{+0.01}_{-0.03}$	−1.14±0.01	$-1.16^{+0.02}_{-0.18}$	−1.59±0.01	$-1.56^{+0.03}_{-0.02}$
$kT_{\rm hot}$ (keV)	(t)	(t)	(t)	(t)	(t)
$\Gamma_{\rm hot}$	1.82±0.01	1.82±0.01	1.79±0.01	1.82±0.01	1.79±0.01
$R_{\rm hot}$ ($R_{\rm g}$)	20±1	20±1	23±1	18^{+6}_{-3}	19^{+8}_{-5}
$kT_{\rm warm}$	0.24±0.01	0.24±0.01	0.24±0.01	0.23±0.01	$0.24^{+0.02}_{-0.01}$
$\Gamma_{\rm warm}$	$2.46^{+0.03}_{-0.04}$	2.45±0.03	$2.42^{+0.02}_{-0.03}$	2.47±0.04	2.44±0.04
$R_{\rm warm}$ ($R_{\rm g}$)	79^{+3}_{-8}	78^{+3}_{-6}	91^{+10}_{-8}	67^{+18}_{-13}	76^{+31}_{-23}
$\log \xi$	(t)	(t)	–	(t)	–
norm(relxill)	$1.9^{+0.4}_{-0.5}\times10^{-5}$	$3.1\pm0.7\times10^{-5}$	–	$1.7\pm0.5\times10^{-5}$	–
χ^2/d.o.f.	1725.0/1610	1726.3/1610	1793.2/1613	1725.4/1610	1789.1/1613
$\chi^2_{\rm red}$	1.07	1.07	1.11	1.07	1.11

Notes. '(t)' means that the value has been tied between both epochs.